Supporting Information

Colossal anomalous Hall effect in the layered antiferromagnetic $EuAl_2Si_2$ compound

*Jie Chen, Xiuxian Yang, Feng Zhou, Yongchang Lau, Wanxiang Feng, Yugui Yao, Yue Li, Yong Jiang, Wenhong Wang**

Supplementary note 1：Composition and crystal structure of $EuAl_2Si_2$.

Energy dispersive X-ray spectroscopy (EDS) and powder X-ray diffraction (XRD) were used to confirm the composition and crystal structure of the samples. As shown in Figure S1 **a**, the colour maps are elemental distributions of the elements Eu, Al, Si. The maps indicate that the elements are uniformly distributed across the surface. And the molar ratio of Eu: Al:Si is approximately 0.93: 2: 2, which is close to the stoichiometric ratio of 1: 2: 2. The powder XRD pattern identified the $CaAl_2Si_2$-type crystal structure (P-3m1 space group). The inset of Figure S1**c** is the photograph of the typical single crystal.

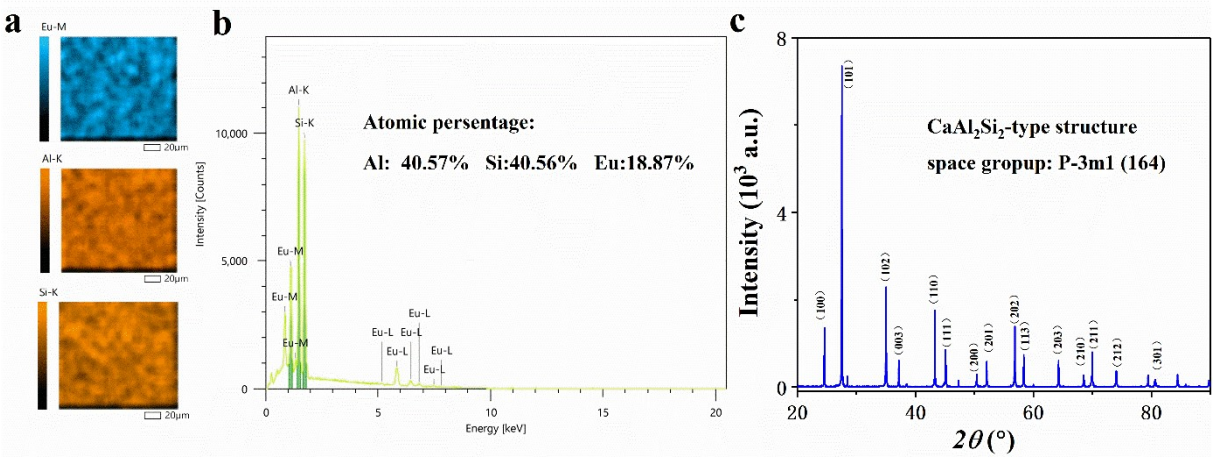

Figure S1 **a** The elemental maps of Eu, Al, Si show that the elemental homogeneity is in the plane. **b** The EDS spectrum of the $EuAl_2Si_2$ single crystal. **c** The powder XRD of the crushed $EuAl_2Si_2$ single crystals at room temperature.

Supplementary note 2：Magnetic properties of $EuAl_2Si_2$ single crytsal.

The antiferromagnetic transition is manifested by the peak in manganisation at about 35 K. The ZFC/FC curves for B // a, b and c show anisotropy at low temperatures. The ZFC/FC curves for B // a and b do not overlap and show an upturn below 24 K. These results suggest that $EuAl_2Si_2$ may have undergone spin reorientation at low temperatures. In the main text, the Curie-Weiss fit for the paramagnetic state indicates that it hosts strong ferromagnetic exchange for the positive θ_{cw}. Combining the neutron diffraction measurements, the dominant interaction is the nearest neighbour ferromagnetic exchange within the ab planes[1], with the weaker antiferromagentic exchange occurring in the interplane. The interplane separation c is much larger than the separation between the Eu ions in the ab-plane. Therefore, the spin reorientation may be due to the competition between ferromagnetic and antiferromagnetic exchange. The magnetic structure at low temperatures requires further experimental investigation. The isothermal magnetisation curves for B // a, b and c show significant anisotropy and the saturation fields are 3 T and 5.8 T, respecctively. Obviously, the c axis is the hard axis and the ab plane is the easy plane.

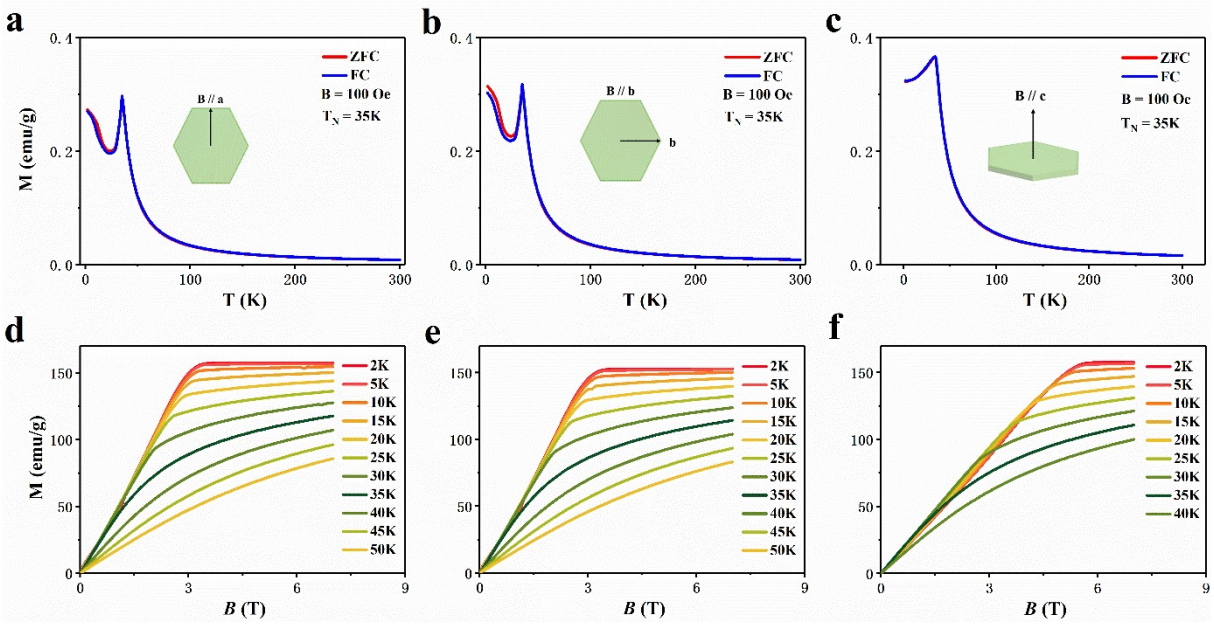

Figure S2 a, **b** and **c** ZFC/FC measurements on temperature dependence of magnetization for *B* // a, b and c directions, respectively, at B = 100 Oe. **d**, **e**, and **f** Field dependence of the magnetisation at low temperatures for B // a, b and c directions, respectively.

Supplementary note 3: Extraction of anomalous Hall resistivity for sample #4.

Here we plot the Hall curves at 2K for sample #4 to show the extraction of the anomalous Hall resistivity ρ_{xy}^{A}. As shown in Figure S3 **a**, we performed a linear fit to the Hall curve above the saturation field and extrapolated the anomalous Hall resistivity at zero field. The negative slope also indicates that the carrier type of this sample at low temperatures is electron. Figure S3 **b** and **d** show the extracted ρ_{xy}^{A} and longitudinal resistivity ρ_{xx} at zero field. ρ_{xy}^{A} decreases with increasing T and changes sign at 12 K. ρ_{xx} increases with increasing T. As shown in Figure S3 **c**, the longitudinal conductivity σ_{xx} initially increases slowly with decreasing temperature and exhibits a kink at the Neel point T_N. For $T < T_N$, σ_{xx} increases rapidly with decreasing T. σ_{xx} reaches $1.18 \times 10^5\ \Omega^{-1} cm^{-1}$ at 2 K.

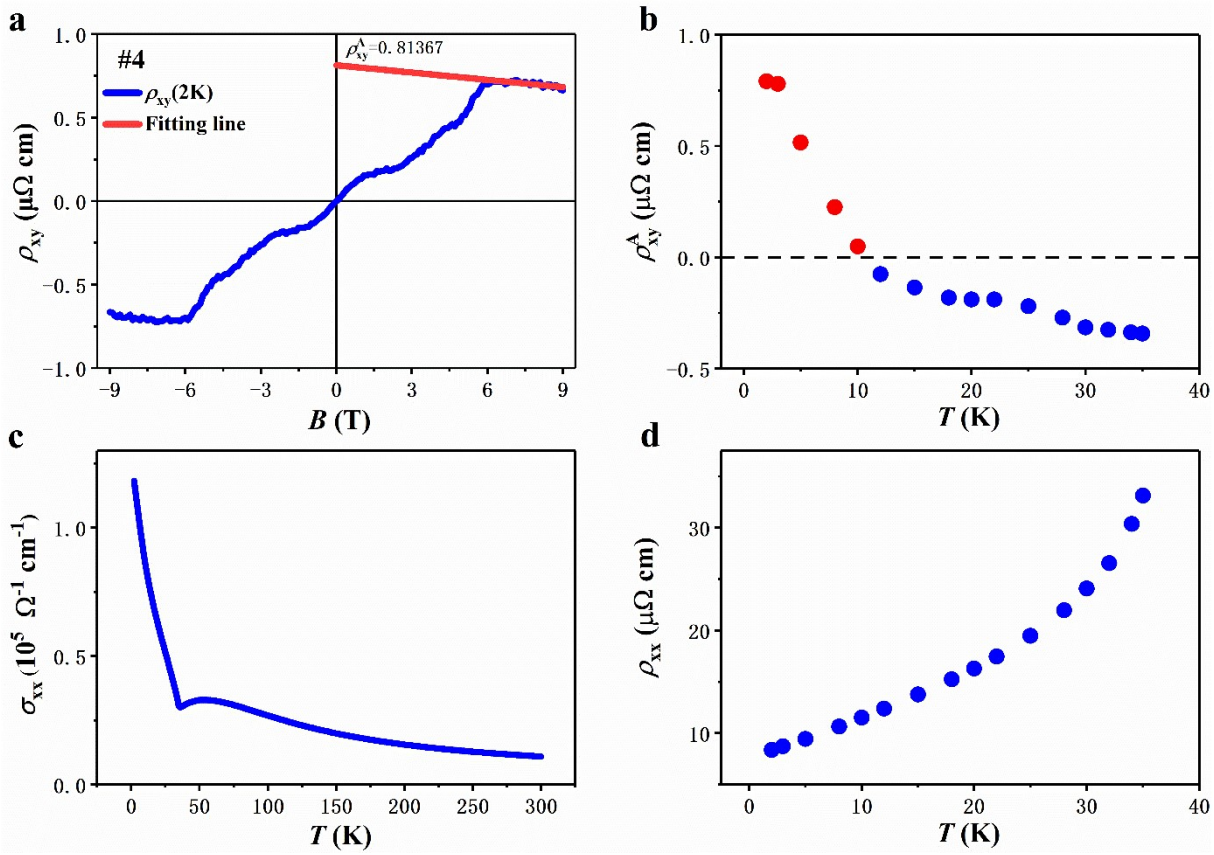

Figure S3 a The Hall resistivity curves for sample #4 at 2K. The red line is the linear fit line. **b** The temperature dependence of the extracted ρ_{xy}^{A}. **c** The temperature dependence of σ_{xx} from 2 K to 300 K. **d** The temperature dependence of the longitudinal resistivity ρ_{xx} at low temperatures.

Supplementary note 4: The Hall resistivity curves for different samples.

Here we provide data on the Hall resistivity of samples #1-#3 and #5-#7. Obviously, samples #1 - #6 shows similar behavior including sign change, topological Hall effect-like anomalous signals at low fields and linear normal Hall resistivity at paramagnetic state. Unlike anomalous Hall signals, topological Hall-like anomalous signals do not change sign with increasing temperature. The negative slope indicates that the electrons dominate the transport for the samples with configuration *B* // c and *I* // b. Interestingly, the dominant carrier type changes when the configuration is *B* // a and *I* // c (sample #7). Another important feature for sample #7 is that the normal Hall effect dominates the Hall curve and masks the anomalous and topological Hall-like anomalous signals contributions. In the low-field region, we can still see the non-linear Hall contribution.

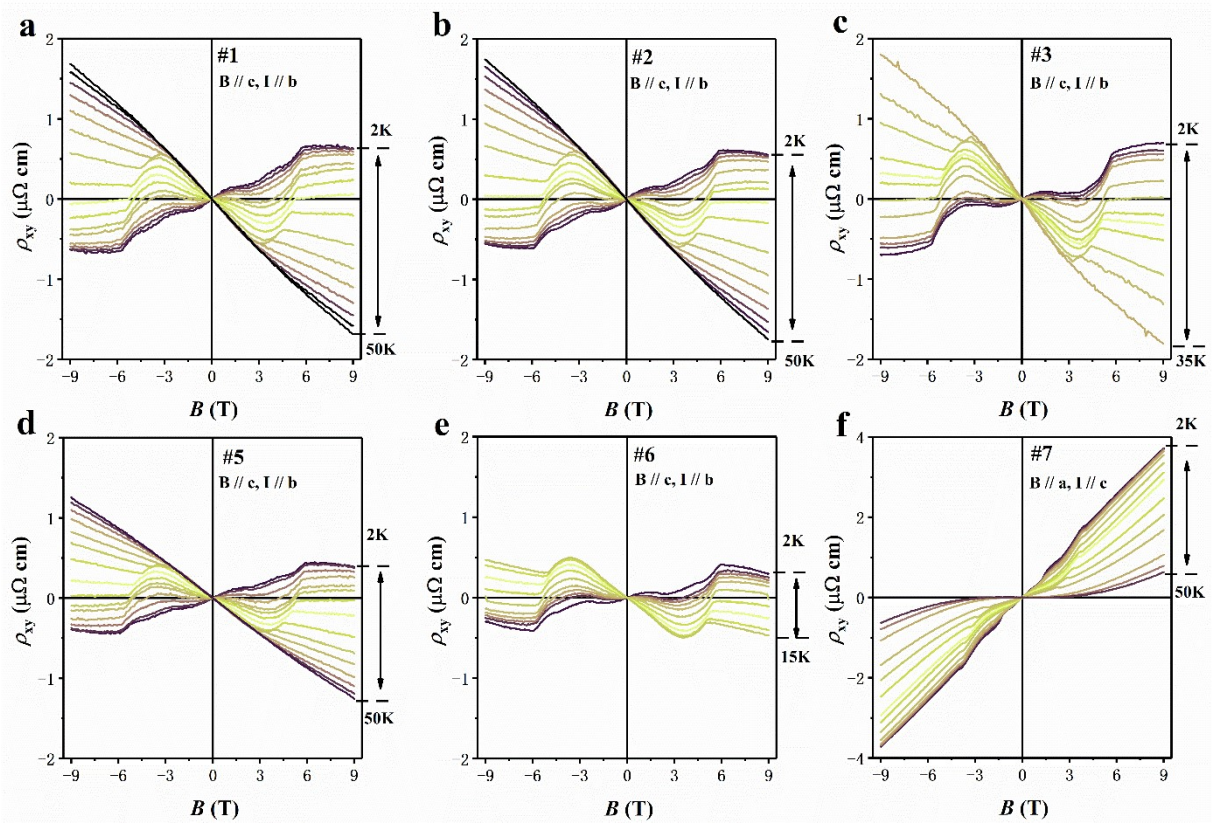

Figure S4 a – **f** are the Hall resistivity curves at different temperatures for samples #1 - #3 and #5 -#7. The configuration of samples #1-6 is that the applied magnetic fields *B* is along to c axis and the electrical current *I* is along to b axis. The configuration of sample #7 is *B* // a and *I* // b.

Supplementary note 5: Extraction of anomalous Hall resistivity for sample #7 and longitudinal conductivity σ_{xx} for samples #3 and #7.

We plot the Hall resistivity curve at 2K for sample #7 in Figure S5 a. The linear fit was also performed above the saturation field. As shown in Figure S5 **a**, the extension of the linear fit curve above the saturation field does not pass through zero point. This suggests that the Hall contribution contains a non-zero anomalous Hall contribution. Figure S5 **b** shows the contribution of the anomalous Hall and the topological Hall-like anomalous signal by subtracting the normal Hall contribution. The extracted anomalous Hall resistivity ρ_{xy}^{A} is plotted in Figure S5 **c**. The sign change also occurred at a certain temperature, similar to that of sample #4. For comparison, we have also plotted the longitudinal conductivity σ_{xx} for samples #3 to #7 in Figure S5 **d**. Obviously, the sample #7 with I // c shows a larger conductivity.

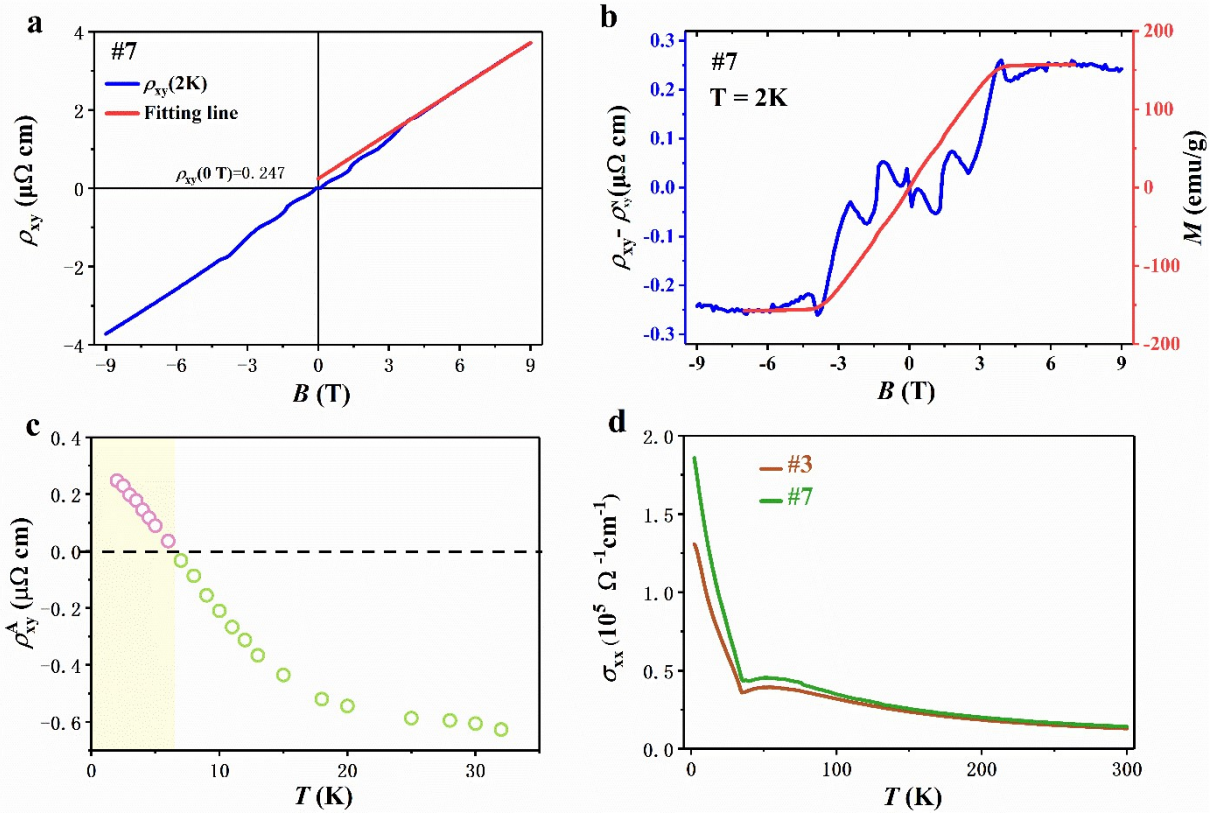

Figure S5 a The Hall resistivity curves for sample #7 at 2K. The red line is the linear-fit line. **b** The Hall resistivity after subtracting the normal Hall part and the isothermal temperature magnetization curves at 2K. **c** Extraction of the anomalous Hall resistivity for sample #7. **d** The longitudinal conductivity for samples #3- #7.

Supplementary note 6: scaling of the anomalous Hall effect.

In the main text, we fit the anomalous Hall conductivity σ_{xy}^{A} versus σ_{xx}^{2} for samples #1 - #6 by $\sigma_{xy}^{A} = a'\sigma_{xx0}^{-1}\sigma_{xx}^{2} + b$, where the data are taken at $T \leq 5K$. As shown in Figure S6 **a**, the parameter a' is distributed at around 0.2. The intercept is also at the order of $10^{4}\,\Omega^{-1}cm^{-1}$. This suggests that there may be other larger contributions in the system, such as side-jump scattering. To explain the sign change between the low and high T, we fit the two parts and extracted the parameters. Compared to the fitted parameters at low temperatures, the fitted parameters at high temperatures changed significantly. a' is lowered, and the sign is changed. The intercept b is about 200 $\Omega^{-1}cm^{-1}$. Therefore, the sign change may arises from the large decay of the skew scattering contribution at high temperatures.

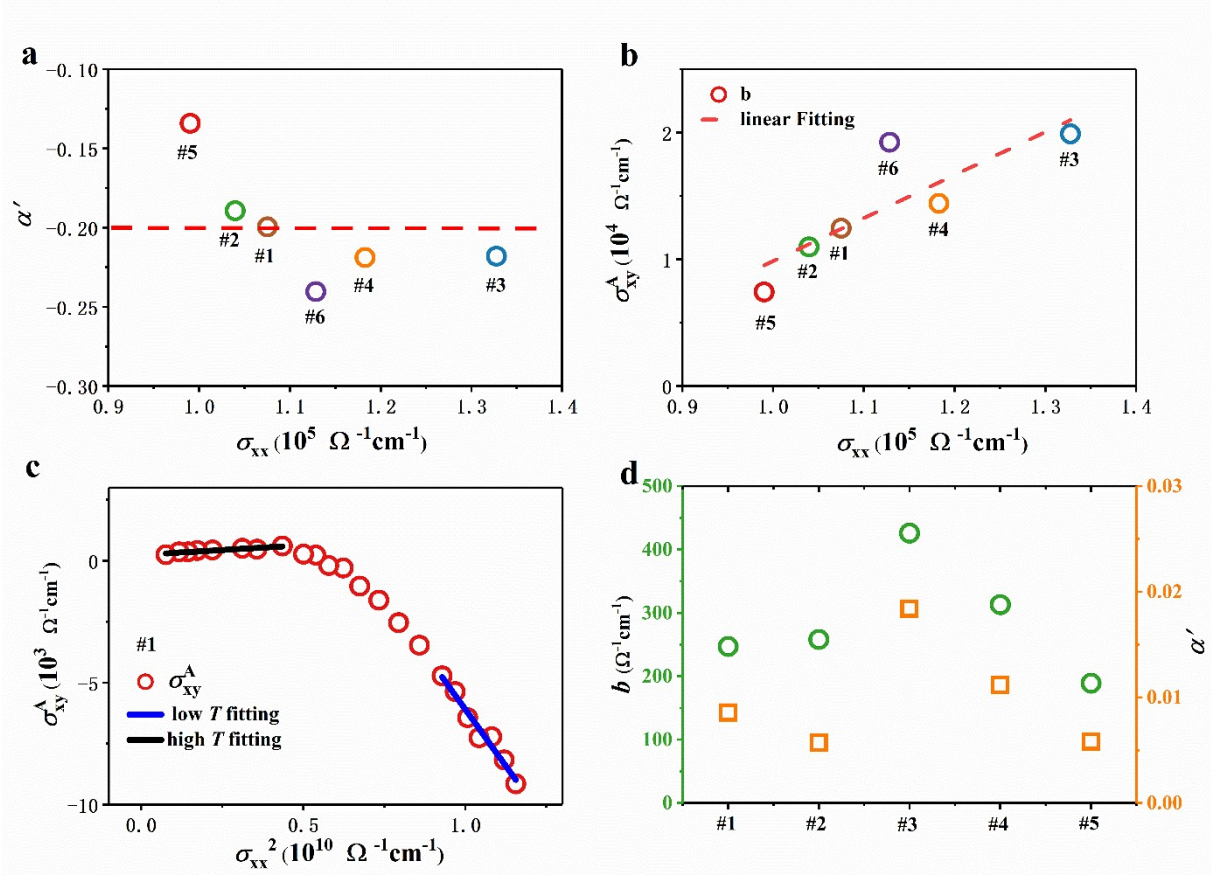

Figure S6 a The parameter a' extracted from the linear fitting for low temperature data. The red dash line is guide line for eyes. **b** The intercept b of a linear fit for samples #1-#6. **c** The fitting for low temperature and high temperatures ($15K \leq T \leq 35K$) for sample #1. **d** The parameter a' and b extracted from high temperature fitting.

Supplementary note 7: Theoretical calculations of band structure and anomalous Hall conductivity with different U.

Here, we investigate the effect of the value of the correlation energy U on the energy band structure as well as on the anomalous Hall conductivity. The influence of different U values on the band structures is that the large value can shift the 4f orbital electron far away from the Fermi energy. As shown in Figure S8, $EuAl_2Si_2$ exhibits the small anomalous Hall conductivity, except for U = 0 eV. Considering the great value of AHC, these results suggest that extrinsic mechanism dominants the anomalous Hall effect of $EuAl_2Si_2$.

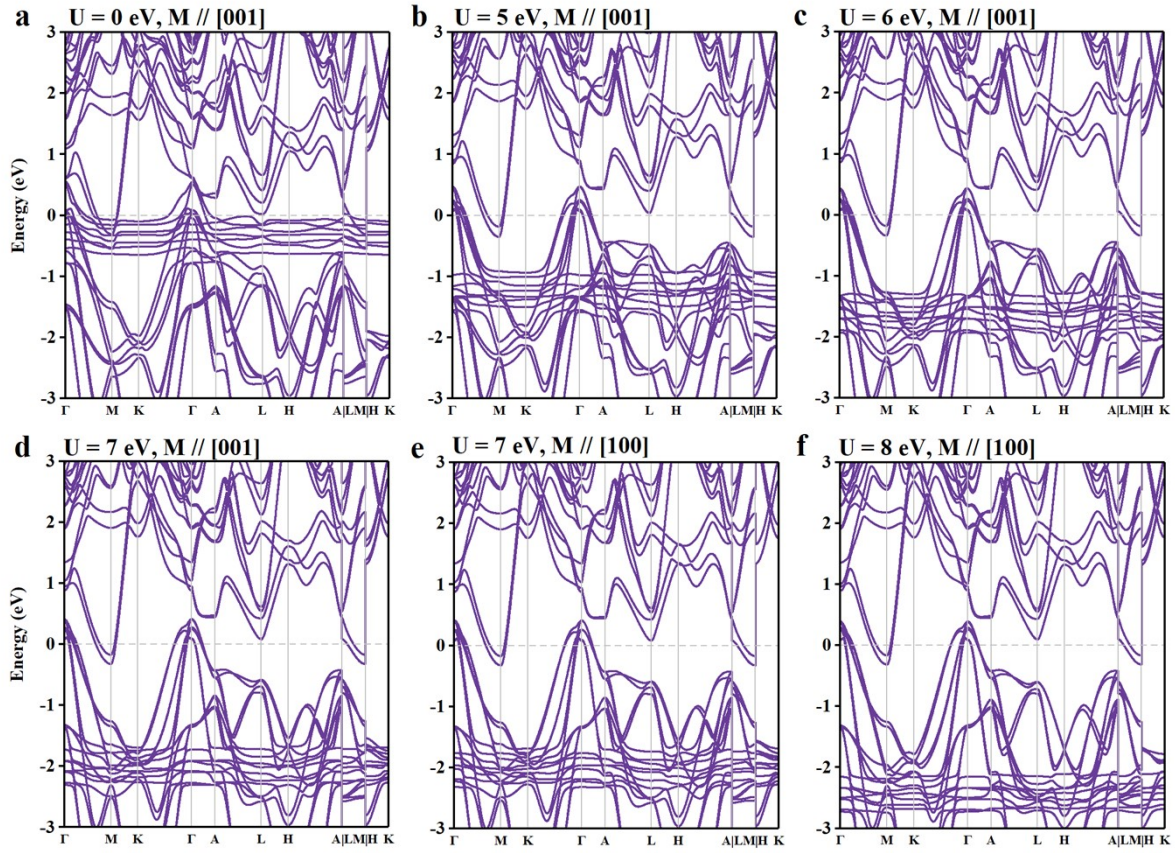

Figure S7 a-d, f The band structure of $EuAl_2Si_2$ alloy along high-symmetry paths with diferent U values and magnetic moment along [100] direction. **e** The band structure with U = 7eV and magnetic moment along [001] direction.

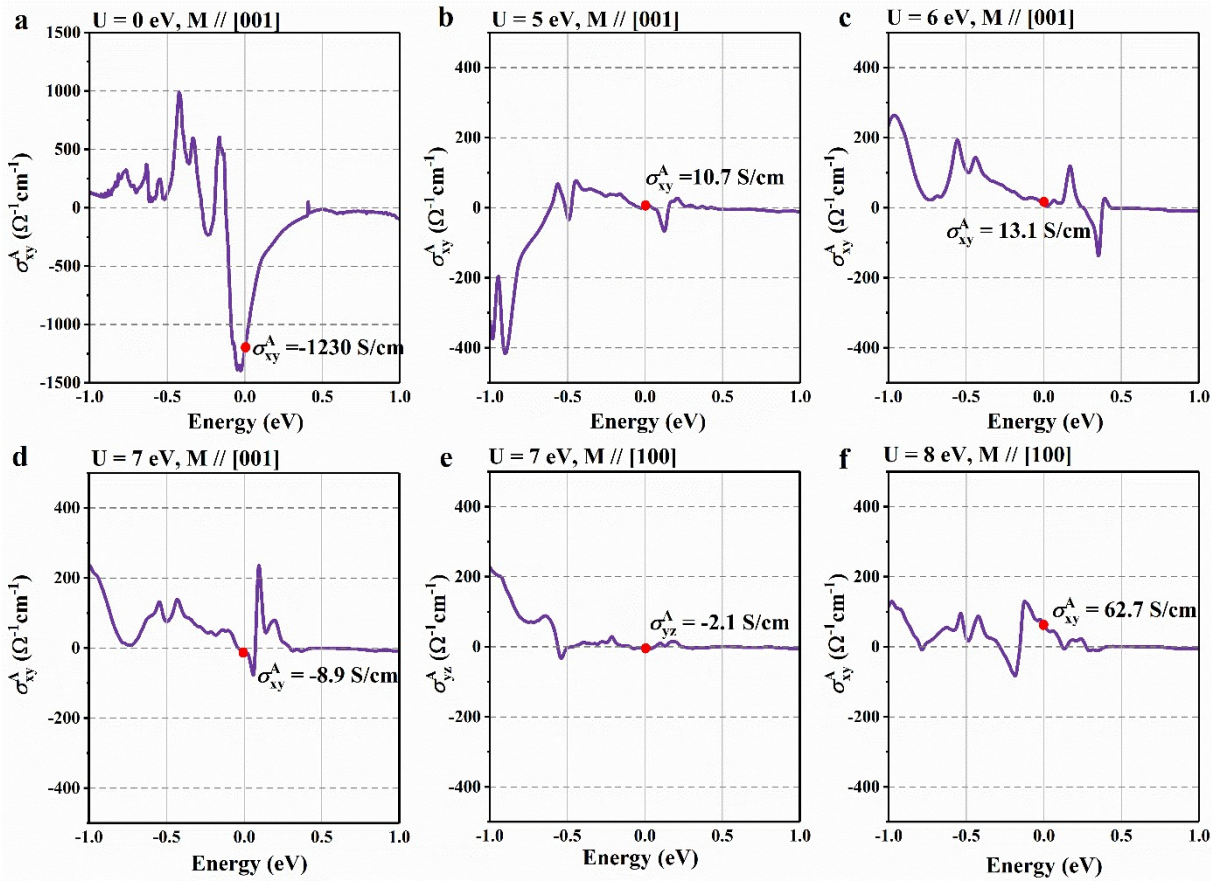

Figure S8 a – f Energy dependence of the anomalous Hall conductivity in terms of the components of Berry curvature.

Supplementary note 8: The contributions of AHC from intrinsic and extrinsic mechanisms.

Based on the previous theoretical work [2], we have attempted to theoretically calculate the intrinsic and extrinsic transport properties of $EuAl_2Si_2$. The scattering-originated contributions (side jump and skew scattering) were incorporating into a short-range Gaussian disorder potential [3]. In the Gaussian disorder model, the skew scattering term comes mainly from the vertex corrections and converges to a finite value in the clean limit. It is therefore called intrinsic skew scattering, which is different from the conventional skew scattering [4]. The anomalous Hall conductivity are calculated using a ultra-dense k-meshe of 300×300×300. The results imply that the intrinsic anomalous Hall conductivity is almost zero for U = 6 eV, but has a large value for U = 0 eV (Figure S9 **c** and **d**). Figure S9 **e** and **f** show the total anomalous Hall conductivity and its decomposition, including the intrinsic, intrinsic skew scattering, and side jump parts for U = 6 eV and 0 eV, respectively. Interestingly, the intrinsic skew scattering contributions are always small. For U = 0 eV (Figure S9 **f**), the side jump shows a large value, but of opposite sign to the intrinsic contribution when the longitudinal conductivity $\sigma_{xx} < 10^5\ \Omega^{-1}cm^{-1}$. These results suggest that the extrinsic contribution in $EuAl_2Si_2$ is rather complex. The conventional skew scattering effect may be responsible for the clossal AHC in our samples.

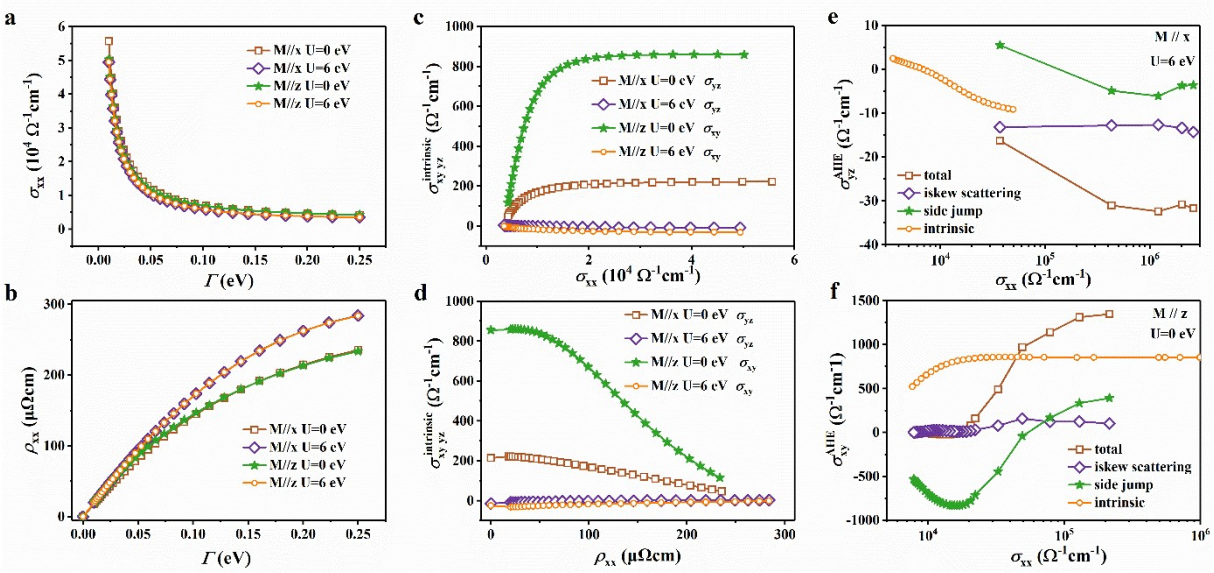

Figure S9 a, **b** The longitudinal conductivity (σ_{xx}) and resistivity (ρ_{xx}) vs disorder parameter (Γ) calculated using the constant smearing model, respectively. **c**, **d** The intrinsic anomalous Hall conductivity as a function of σ_{xx} and ρ_{xx}, respectively. In **a**-**d**, the brown squares (purple diamonds) and green pentagrams (orange circles) represent the spin moments along the x and z directions, respectively, at U=0 (6) eV. **e, f** Dependence of the total anomalous Hall

conductivity and its decomposition (intrinsic, side jump, and intrinsic skew scattering) on σ_{xx} when U = 6 eV and 0 eV, respectively.

Supplementary note 9: Density of states and Fermi surfaces of $EuAl_2Si_2$.

In order to further analyse the composition of the band structure near the Fermi level, we have carried out detailed calculations of the density of states. The results indicate that the density of states near the Fermi level originates mainly from the contribution of Al and Si atoms and a small amount of Eu atoms. And further analyses show that the contributions originate mainly from the s and p orbitals of the Al atom, p orbital of Si and d orbital of Eu. Figure S10 **c** shows the fermi surfaces of $EuAl_2Si_2$. For the spin-up energy bands, there are three bands that cross the Fermi level. The band at M point forms the α fermi surface. The two bands crossing Γ point forms the β and γ fermi surfaces.

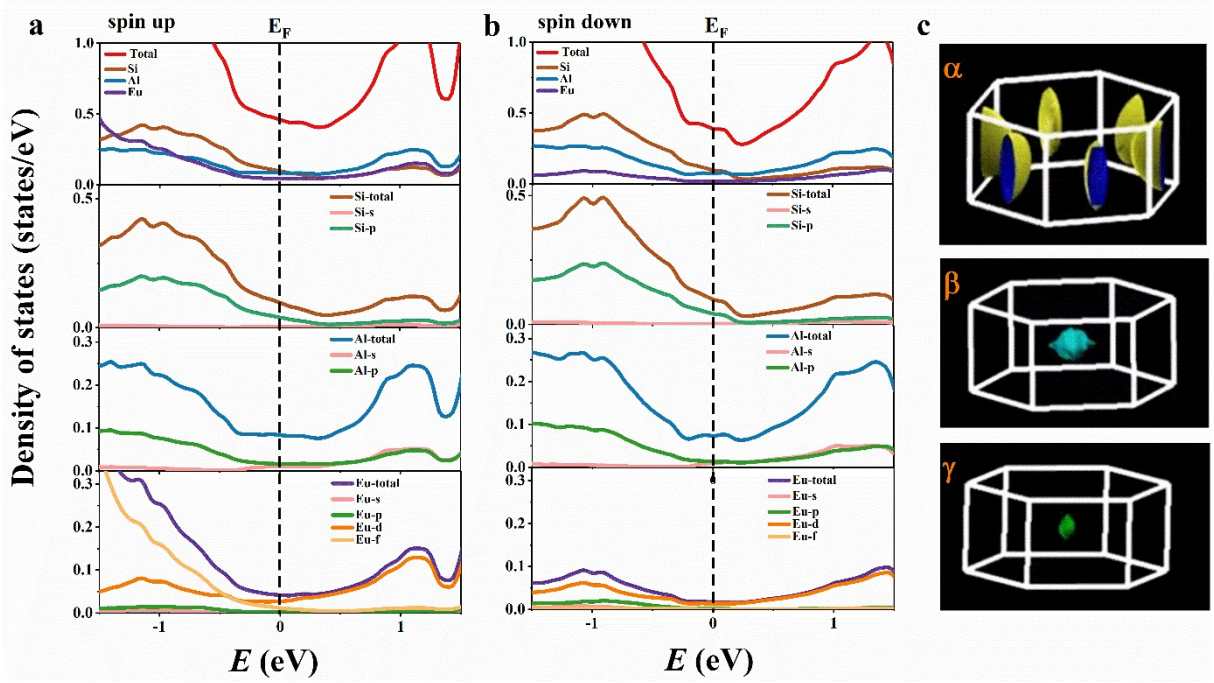

Figure S10 a Density of states of $EuAl_2Si_2$ with spin up. **b** Density of states of $EuAl_2Si_2$ with spin down. **c** Fermi surfaces of $EuAl_2Si_2$ with spin up.

[1] P. Schobinger-Papamantellos, F. Hulliger, *Journal of the Less-Common Metals* **1989**, 146, 327.

[2] X. Yang, W. Feng, X.-P. Li, G.-B. Liu, Y. Mokrousov, Y. Yao, *Phys. Rev. B* **2023**, 107, 224405.

[3] P. Czaja, F. Freimuth, J. u. Weischenberg, S. Bl¨ugel, Y. Mokrousov, *Phys. Rev. B* **2014**, 89, 014411.

[4] a) N. A. Sinitsyn, A. H. MacDonald, T. Jungwirth, V. K. Dugaev, J. Sinova, *Phys. Rev. B* **2007**, 75, 045315 ; b) N. A. Sinitsyn, *J. Phys.: Condens. Matter* **2008**, 20, 023201.